An Advanced Time-Series InSAR Approach Based on Poisson Curve for Soft Clay Highway Deformation Monitoring

Lingjie Zhu , Xuemin Xing , Yikai Zhu , Wei Peng, Zhihui Yuan , *Member, IEEE*, and Qing Xia

Abstract—Monitoring surface deformation for highways built on soft clay subgrades is fundamental for understanding the dynamics of the settlement process and preventing the occurrence of safety accidents. Most of the traditional interferometric synthetic aperture radar (InSAR) deformation models for highway monitoring are based on a combination of one or several empirical functions, which ignores the underground mechanism of highway deformation. To overcome this limitation, we proposed an advanced InSAR approach that improved the InSAR deformation model and parameter estimation algorithm for soft clay road deformation monitoring. The improved InSAR deformation model is based on the Poisson curve, which considers the characteristics of the temporal physical deformation evolution of the soft clay. The improved algorithm for the unknown parameter estimation is based on a GARN algorithm, which can solve the parameters with better accuracy by combining the genetic algorithm and the regularized Newton iterative algorithm. To evaluate the better performance for the proposed approach and its feasibility for soft clay highway monitoring, both the simulation and the real data experiments on a soft clay highway in Foshan, China, are performed. The time-series deformation from January 1, 2015 to January 18, 2017, is retrieved, and the temporal deformational characteristics over this area are analyzed, which facilitates a greater understanding of the deformational evolution process of the soft clay highway. The results are verified in terms of the residual high-pass deformation and the final obtained vertical deformation compared with the external leveling measurements, which indicate the greater reliability of our method.

Index Terms—Deformation model, genetic algorithm (GA), interferometric synthetic aperture radar (InSAR), soft clay, time-series deformation.

Lingjie Zhu, Xuemin Xing, Yikai Zhu, Wei Peng, and Qing Xia are with the School of Traffic and Transportation Engineering, Changsha University of Science and Technology, Changsha 410114, China, and also with the Laboratory of Radar Remote Sensing Applications, Changsha University of Science and Technology, Changsha 410114, China (e-mail: zzzhu@stu.csust.edu.cn; xuemin.xing@csust.edu.cn; kai@stu.csust.edu.cn; pengwei@csust.edu.cn; xiaqingfriendxia@126.com).

Zhihui Yuan is with the School of Electrical and Information Engineering, Changsha University of Science and Technology, Changsha 410114, China, and also with the Laboratory of Radar Remote Sensing Applications, Changsha University of Science and Technology, Changsha 410014, China (e-mail: yuanzhihui@csust.edu.cn).

Digital Object Identifier 10.1109/JSTARS.2021.3100086

I. Introduction

WITH the geotechnical characteristics of high natural water content, high compressibility, low intensity, and poor structure, the soft clay subgrade is highly prone to cumulative deformation and instability settlement [1]–[3]. Stability control of the man-made infrastructures built on soft soil has become a major technical problem in highway engineering. Consequently, the long-term settlement monitoring of soft clay highways during the postconstruction period is of great engineering significance to prevent the occurrence of safety accidents and ensure the quality of highway construction [4].

Differential interferometric synthetic aperture radar (D-InSAR) has been widely applied to ground surface movement monitoring with its advantages of large spatial coverage, high imaging resolution, and nonintrusive surveying. Its complement to the traditional geodetic surveying methods has been adequately proven [5]–[7]. However, the accuracy of D-InSAR derived deformation can be unavoidably influenced by its well-known spatial–temporal decorrelation and atmospheric delay [8]–[10]. Multitemporal InSAR (MT-InSAR) technology, such as persistent scatterer interferometric synthetic aperture radar (InSAR) [11] and small baseline subset InSAR (SBAS-InSAR), is an extended advanced InSAR technology, which has been gradually developed and widely applied to the ground movement detection and deformation investigation with millimeter precision [12]. The potential of MT-InSAR has been investigated for measuring the ground time-series deformation over those man-made infrastructures, such as railways, highways, and bridges, thus showing the high-potential ability for the application to large traffic infrastructures [13]–[20].

In the process of InSAR data processing, deformation modeling is a crucial step, which builds the temporal and functional relationships between the interferometric phase component of the displacement and the deformation parameters. Most of the InSAR deformation models for highway monitoring are based on the combination of single or several empirical models (such as the linear model [21], seasonal model [22], and polynomial model [23]), lacking the specific deformation mechanism of the highway subgrade. Those pure mathematical empirical models may not accurately describe the real time-varying disciplines of the settlement of highway soft soil foundation, which would not only affect the accuracy of the derived time-series deformation but also bring difficulties to the following displacement

interpretation. Generally, the settlement process of the soft soil follows the three periods of occurrence, development, and stability, and then reaches a steady state, which can be described as an inverse "S" curve [24]. With the characteristics of monotonous increasing, boundedness, and reverse point of inflection, the Poisson curve is a typical "S" type growth curve and has been proven that can accurately reflect the temporal variations of the consolidation process for soft soil subgrade. The Poisson curve has been widely used in the field of highway postconstruction prediction [24]–[27]. Consequently, to describe the temporal evolution process of soft soil deformation with better reality, the Poisson curve is introduced here into the traditional MT-InSAR deformation modeling and an advanced time-series InSAR deformation model based on the Poisson curve is proposed for the soft clay highway deformation monitoring.

After InSAR deformation modeling, the model parameter estimation step should be carried out. The estimation of the parameters for the advanced InSAR deformation model based on the Poisson curve is a typical nonlinear parameter estimation problem. The genetic algorithm (GA) has been introduced to InSAR parameter estimation and has been proven to be feasible in solving the problems of nonlinear parameter estimation [29]. Since GA is insusceptible to the specific functional form of the model, it is more suitable for solving those complex nonlinear functions. However, GA has the disadvantages of low accuracy and long-time processing [30]. Another kind of nonlinear parameter estimation algorithm is based on the nonlinear least square algorithm (NLSA) that obtains the estimation with an iterative resolution. Those kinds of algorithms can obtain the parameters with better efficiency than that of GA searching. However, the accuracy of NLSA highly depends on the setting of the initial parameters. The large deviation between the initial values and the real parameters may lead to a slow iterative process or even nonconvergency [31]. Consequently, an improved algorithm, namely GARN, based on the combination of GA and the regularized Newton (RN) iterative algorithm, is proposed, which can integrate both the advantages of the two algorithms combinedly. By searching the global optimal solutions with GA, the regularization initial value can be obtained. Then, the GA-generated initial value is optimized by the RN, which can generate an optimized estimation for the model parameters.

As discussed above, in this article, we propose an advanced InSAR approach for soft clay highway deformation monitoring. In the approach, both the InSAR deformation model and the parameter estimation algorithm are improved. The SBAS-InSAR technique and the InSAR deformation modeling based on the Poisson curve are briefly introduced in Section II. Then, the principles of GARN and the processing flow of our new approach are introduced. The simulation and real data experiments based on the Poisson curve and GARN are introduced in Sections III and IV, respectively, and the characteristics of the obtained time-series deformation are discussed. Finally, Section V concludes this article and the residual deformation and comparison with external leveling measurements are discussed to verify the better performance and feasibility for soft clay highways.

II. METHODOLOGY

A. Linear Model of the Traditional SBAS-InSAR Technique

Suppose $N + 1$ SAR images covering the same area are acquired in repeat orbit at different dates. Then, according to certain spatial–temporal baseline thresholds, N interferometric pairs are generated, whereas M interferometric pairs are generated through the two-orbit D-InSAR processing (satisfying the inequality $\frac{N}{2} \leq M \leq \frac{N(N-1)}{2}$). The unwrapped differential interferometric phase can be written as follows [32], [33]:

$$\delta\phi_j(x, r) = \phi_B(x, r) - \phi_A(x, r)$$
$$\approx \frac{4\pi}{\lambda}[d(t_B, x, r) - d(t_A, x, r)]$$
$$+ \Delta\phi_{\text{topo}}^j(x, r) + \Delta\phi_{\text{res}}^j(x, r) \qquad (1)$$

where $j \in (1, \ldots, M)$ represents the index of interferograms; λ is the wavelength; $d(t_B, x, r)$ and $d(t_A, x, r)$ represent the cumulative displacement along the radar line of sight (LOS) direction at dates t_B and t_A with respect to $d(t_0, x, r) = 0$, respectively. $\Delta\phi_{\text{topo}}^j(x, r)$ defines the residual terrain phase, which can be expressed as $\Delta\phi_{\text{topo}}^j(x, r) = \frac{4\pi B_\perp}{\lambda R \sin\theta} \Delta h(x, r)$; $B_\perp$ defines the spatial baseline; R is the range between the sensor and ground object; θ is the incidence angle; Δh represents the elevation correction; $\Delta\phi_{\text{res}}^j(x, r)$ defines the residual phase component, which is related to noise, atmospheric delay, and high-pass (HP) deformation.

According to the article presented in [34], the linear deformation model assumes that the displacement for each time-adjacent interferometric period follows a linear variation. The functional relationship can be written as

$$d(t_B, x, r) - d(t_A, x, r) = v_j \cdot (t_B - t_A) \qquad (2)$$

where v_j defines the linear velocity for each temporal unit and varies in different temporal units. Substituting (2) into (1), the unknown parameters are the linear velocities in different periods and the elevation correction. The solution of the unknown parameters is an LS problem. Since the equation coefficient matrix is a typical singular matrix, the singular value decomposition method can be used to estimate the linear rate for each period [13], and then the settlement value can be obtained by integrating the velocity of each period, and the final linear time-series deformation results can be obtained.

B. Time-Series InSAR Deformation Model Based on the Poisson Curve

As shown in Fig. 1, the Poisson curve is a typical "S" type growth curve, which can accurately reflect the varying disciplines of the soft soil consolidation process. It has been widely applied to the deformation prediction of soft soil subgrade and pavement [24]. The Poisson function can be expressed as

$$W(t) = \frac{W_0}{1 + ae^{-bt}} \qquad (3)$$

where $W(t)$ is the dynamic ground subsidence at time t with respect to the reference time $t_0 = 0$. W_0 denotes the possible
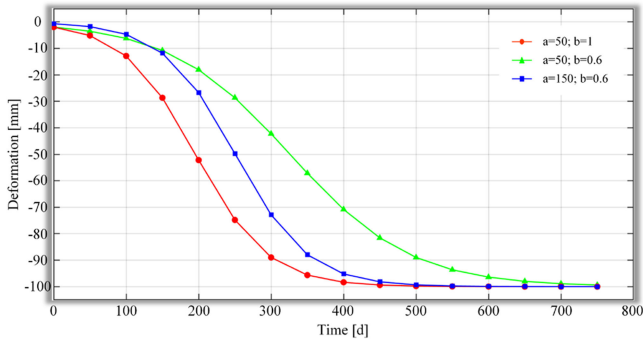
Fig. 1.   Example of the Poisson curve at a ground point.

maximum subsidence. a and b are the shape parameters of the curve. Fig. 1 shows an example of the Poisson curve on a single point from which we can see that the higher the a is, the longer the initial subsiding time at the ground point lasts and the longer the time to reach the maximum subsidence value. The higher the b is, the faster the subsiding rate of the ground point is and more obviously the shape of the curve varies [35]. Ignoring the influence of horizontal movement, the LOS deformation monitored by InSAR is converted into vertical time-series deposition following $W = \frac{d_{\text{LOS}}}{\cos \theta}$ (where θ is the radar incidence angle) [36]. Equation (3) can be rewritten as

$$d_{\text{LOS}}(t) = \frac{W_0}{1 + ae^{-bt}} \times \cos \theta. \tag{4}$$

Substituting (4) into (1), we can get

$$\delta \phi_j = \frac{4\pi \cos \theta}{\lambda} \left[\frac{W_0}{1 + ae^{-bt}B} - \frac{W_0}{1 + ae^{-bt}A} + v(t_B - t_A) \right]$$

$$+ \frac{4\pi}{\lambda} \frac{B_\perp \Delta h}{R \sin \theta} + \Delta \phi_{\text{res}}^j \tag{5}$$

suppose N interferometric pairs generated, the unknown parameters here are the Poisson curve parameters (W, a, b), linear rate v, and elevation correction Δh. When the number of equations is higher than or equal to 5, the unknown parameters over all the high-coherence points can be estimated.

C. Genetic Algorithm

The GA is a method based on globally optimized searching that is insusceptible to both the number of unknown parameters and the specific form of the model. The basic idea of the GA is to obtain the population individuals as the final solution of the parameters, which can satisfy the condition of minimizing the fitness function through the operations of selection, crossover, and mutation [37]. According to (5), each gene of a population includes the Poisson curve parameters (W, a, b), the linear velocity v, and the elevation correction Δh. The fitness function is mainly modeled following the residual minimum norm principle, which can be expressed as follows:

$$f = ||\Delta \phi_{\text{res}}^j|| = \min \tag{6}$$

where $\Delta \phi_{\text{res}}^j$ represents the residual phase in (6). The general searching procedure includes the following steps: First, the

magnitude of each initial individual gene should be set, that is, the initial range of each unknown parameter needs to be fixed. Simultaneously, the corresponding fitness function value of each gene can be calculated; then, whether the iteration termination condition for the minimum fitness function is satisfied should be determined. If not, the subsequent process of selection, crossover, and mutation for the individual population should be carried out to obtain a new individual population, and the fitness function value will be calculated repeatedly. This iteration process is terminated when the iteration termination condition for the minimum fitness function is satisfied. Finally, the generated individual genes will be selected as the final estimated parameter.

D. RN Iteration Algorithm

The iterative formula of the ordinary Newton iterative algorithm is as follows:

$$x^{(k+1)} = x^{(k)} + dx^{(k)} = x^{(k)} - G_k^{-1}(g^{(k)})^t \tag{7}$$

where G_k is the iterative matrix at $x^{(k)}$, which should be non-singular for the ordinary Newton iterative algorithm. Practically, when G_k is almost singular or even seriously ill, its inverse matrix will be unstably unavoidable, and the iterative format of (7) is no longer applicable. As introduced in [38], the ill-condition of the matrix can be improved by the regularization algorithm, which replaces the iterative matrix by adding a vector matrix $\alpha^k I$ (where α^k is named the regularization factor), i.e., $G_k + \alpha^k I$ instead of G_k in (7). The ill-condition of the original iteration matrix can be improved based on an appropriate selection of α^k. Accordingly, the stability of the inverse operation of $G_k + \alpha^k I$ can be effectively guaranteed, and the iteration process can be carried out more smoothly. The Newton iterative function of regularization can be written as

$$x^{(k+1)} = x^{(k)} + dx^{(k)} = x^{(k)} - (G_k + \alpha^k I)^{-1}(g^{(k)})^t. \tag{8}$$

The condition number of a matrix is an important index to measure the ill-condition level of the matrix. The addition of $\alpha^k I$ in the upper version can significantly reduce the condition number of G_k, thus improving the situation of nonconvergence iteration caused by the ill-condition of the iterative matrix.

E. Combination of GA and the RN Iterative Algorithm (GARN)

As introduced in [37], GA searching results may contain large amount of random errors induced by premature convergent searching, which means the genes may not converge to the global optimal solutions at the end of the iteration. Comparatively, the accuracy of estimation generated by a singular RN iterative algorithm significantly depends on the set of the initial values of the unknown parameters [38]. If a high deviation between the preset initial magnitude and the true values exists, the iterative process will be slow or even nonconvergency. Therefore, we propose a GARN algorithm, which can consider both the advantages of the two algorithms combinedly. By searching the global optimal solutions with GA, the rough global optimal solutions for the unknown parameters can be obtained, which will be used as the initial input value subsequently. Then, the GA-generated initial values are secondarily refined by the RN, which can
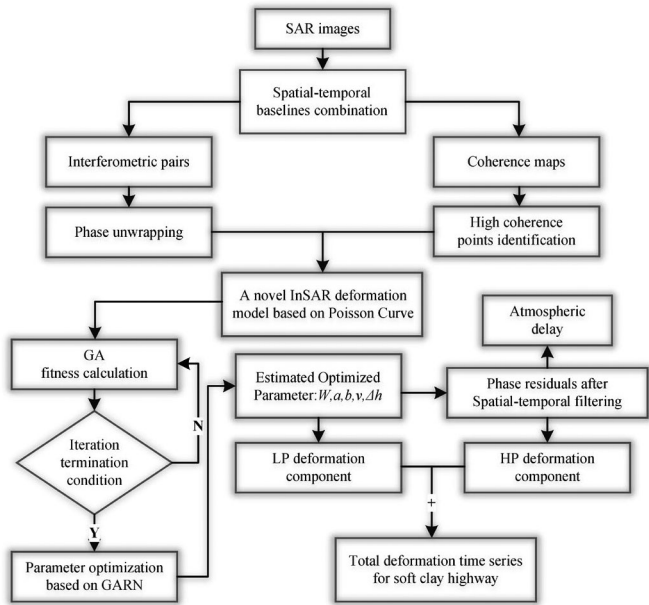
Fig. 2. Processing flow of the advanced time-series InSAR approach based on the Poisson curve for soft clay highway deformation monitoring.

generate optimized estimations for the unknown parameters of the deformation model.

F. Advanced Time-Series InSAR Approach Based on the Poisson Curve

Fig. 2 illustrates the general processing flow of the advanced time-series InSAR approach based on the Poisson curve for soft clay highway deformation monitoring. The basic steps are as follows:

1) generating unwrapped differential interferograms over the study area;
2) selecting the high-coherence points based on the indices of the average correlation coefficient, intensity, and amplitude dispersion;
3) InSAR deformation modeling based on the Poisson curve, which builds the temporal functional relationship between the InSAR phases and the unknown parameters;
4) GARN parameter estimation, which includes generating the initial values of the unknown parameters based on the GA global searching and secondary optimization by the RN iterative algorithm.
5) total deformation time-series generation, including the summarization of the LP deformation and the HP deformation obtained by residual phase filtering.

III. SIMULATED EXPERIMENT

To verify the feasibility and reliability of the aforementioned advanced approach, a simulated experiment was designed. The range of the maximum subsidence W_0 was set within $[-80, 20]$ mm, whereas the linear velocity v within $[-20, 10]$ mm/yr. The Poisson shape parameters a and b were set within the range of $[0, 200]$ and $[0, 50]$, respectively. The real

parameter field of a and b was simulated by a two-dimensional Gaussian function model. The elevation correction Δh was simulated through the Gaussian random simulator with the value controlled within the range of $[-50, 50]$ m. Linear velocity was simulated using the MATLAB peak function, which can satisfy both positive and negative distribution characteristics of displacement [39]. In order to evaluate the performance of parameter estimation in conditions of different numbers and network connectivity of interferograms, two groups of simulated experiments were carried out. The first group was under single-master connectivity, which means only one-master image is selected and the rest ones are connected to it. The second group was under multimaster connection, with multimaster images selected based on a small baseline principle. For both groups, the total numbers of interferograms were set as 10, 15, 20, 25, and 30. The satellite parameters were set according to the known SAR sensor parameters (TerraSAR-*X*-band, Stripmap descent mode), including spatial and temporal baselines of each interferometric pair. There were 600 high-coherence points generated in the simulation. The parameter values over the 600 high-coherence points were randomly extracted from the simulated parameter field as true values, which were used to verify GARN-generated estimations. Fig. 3 shows the accumulated time-series deformation compared with the simulated true deformation sequences, and the differences between them are shown in the last figure. It can be clearly seen from the figure that, compared with the green polylines, the blue polylines show better consistency (closer to the red polylines), and the differences generated by the two algorithms are demonstrated in the last figure of Fig. 3. The results indicate that the model parameters obtained by GARN display a better accuracy. To quantitatively compare the accuracy between the two algorithms, the root-mean-square error (RMSE) for each model parameter was calculated. The RMSEs of all the five unknown parameters were lower than 5% of the estimated maximum magnitudes. Comparatively, the RMSE of unknown parameters estimated by GARN was significantly improved, with an increment of 46.7% for W_0, 68% for a, 46.3% for b, 57.0% for v, and 59.9% for Δh, respectively.

Fig. 4 shows the quantitative comparison of RMSE for each parameter based on our proposed InSAR approach under different interferometric numbers and network connections. We can infer from the figure that for both the two different network connections, the RMSE of W_0, a, and v in the Poisson model shows a relatively higher sensitivity to the number of interferograms, among which W_0 is the most sensitive parameter. For both two groups, RMSEs of the three sensitive parameters decrease with the increase of the total number of interferograms. As the number of interferograms increases from 10 to 30, the RMSE of W_0 is reduced from 15 to 8.4 mm, with an improvement of 44% under the single-master connection. In contrast, b and Δh display a stable state when the number of interferograms varies. As the number of interferograms increases from 10 to 30, the RMSE of Δh varies from 1.92 to 1.86, almost the same. It can also be noted that under the multimaster connection network, the accuracy of solving the unknown parameters of the Poisson model is generally higher than that of a single-master-image
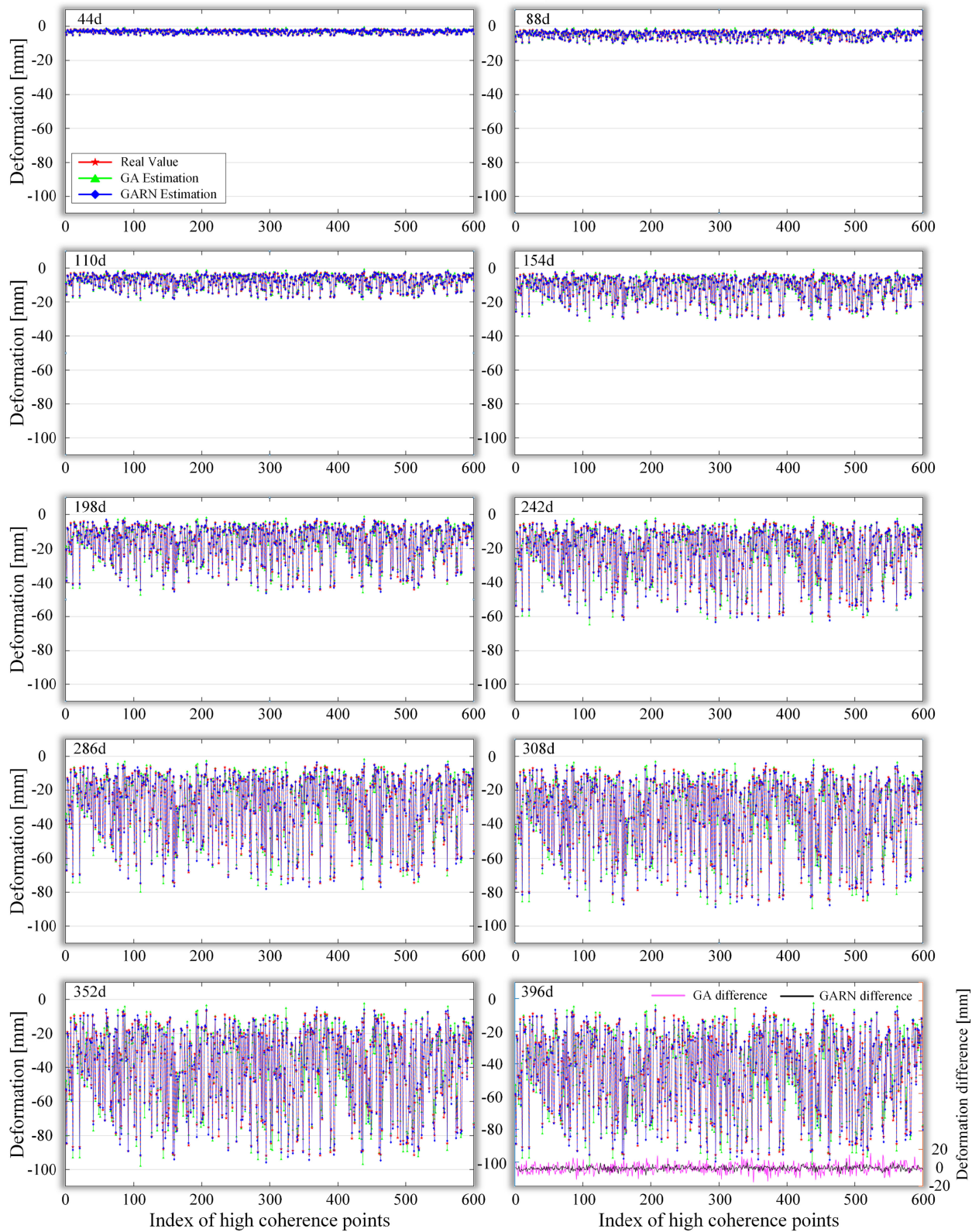
Fig. 3. Comparison of the time-series settlement obtained by GA and GARN with the simulated true value (*d*: days).
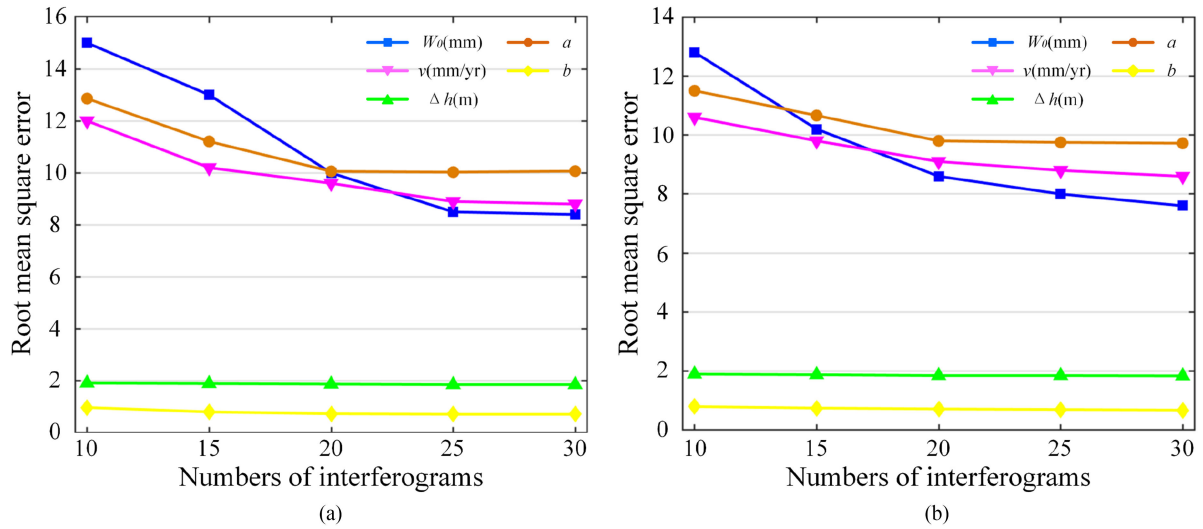
Fig. 4. RMSE for each parameter under different interferometric numbers. (a) Single-master connection. (b) Multimaster connection.
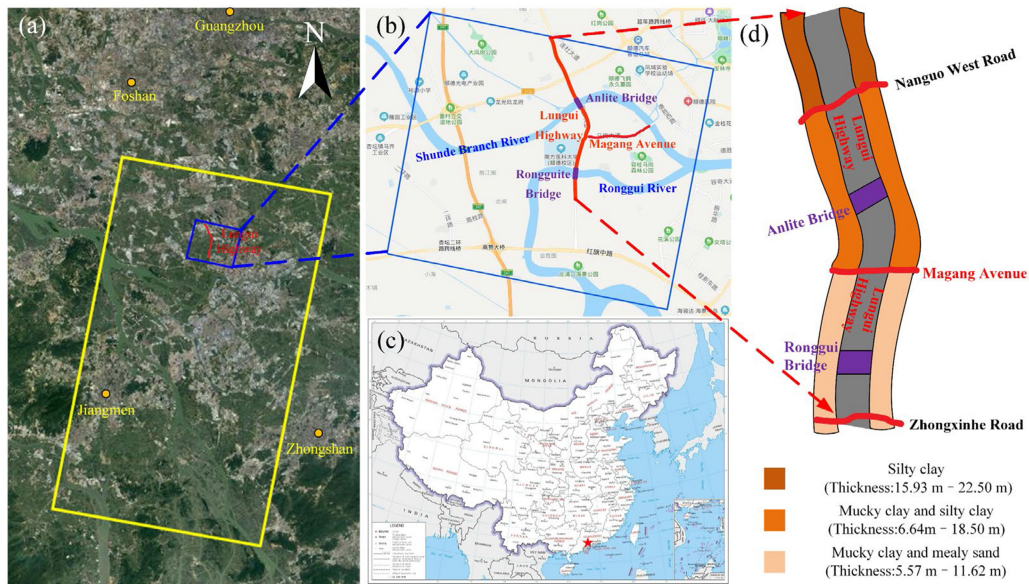

Fig. 5. Study area featured at different scales. (a) TerraSAR-X image coverage. (b) Location of Lungui Highway. (c) Geological distribution of the soft soil along the longitudinal direction of the Lungui Highway.

connection. Consequently, a relatively total number higher than 25 and multimaster connectivity should be suggested in the real data experiment when adopting our approach.

IV. REAL DATA EXPERIMENT

A. Study Area

The test area selected here is a stretch of highway, namely Lungui Highway, located in Foshan, Guangdong Province, China. The design width of the roadbed is 60 m and the total length is about 12 km. The construction of the Lungui Highway is started in March 2011. It was opened to traffic segmentally during the construction process, and the whole route officially opened to traffic in January 2015. Fig. 5 shows the study area, featured at different scales. As shown in Fig. 5(b), the Lungui Highway is located close to two hydrological systems: the Rongui and Shunde Branch River. Plenty of ponds and a large amount of silt are distributed along the route. Lungui Highway is an important link in the Foshan transportation system, Hongqi Middle Road, Nanguo West Road, Guangzhou Ring Expressway, and Longzhou Highway northward. It is one of the three major north–south traffic arteries in Foshan. For the significant traffic situation of the Lungui Highway, the passenger flow volume was extremely huge (up to 2295.21 million people/km in 2017 according to the statistics of the Fuoshan Transportation Bureau). According to the collected geological material, with a developed surface water system and extensive aquifers, the soft soil covering the upper layer is extremely soft and with

high compressibility. Delta alluvial and silt plain dominate the topography of the area. The surface quaternary over this area is mainly composed of silty soil and mealy sand, deposited by sea and land, including mucky clay, silty soil, and mealy sand. With the characteristics of high water content, high compressibility, low mechanical intensity, and high sensitivity, the subgrade of the highway is highly prone to liquefaction and seismic subsidence. Consequently, the long-term stability monitoring over this area is of great necessary.

Fig. 5(d) is a longitudinal sectional view of the test section. The main distribution characteristics of the rock and soil layers along the Lungui Highway are artificial cohesive plain fill and Quaternary Holocene sea–land alternate strata. The overlying Quaternary system is mainly composed of silty soil and silt fine sand deposited by sea and land alternate facies, specifically including silty clay, silty soil, and silt. From the perspective of the longitudinal distribution of the soft soil layer, the soil on the north section of Nanguo West Road is dominated by continuously distributed silty clay, and the thickness of the soft soil layer is 15.93–22.50 m; the segment from Nanguo West Road to Magang Road is soft soil. The layer is dominated by continuously distributed silty soil and silty clay, and the thickness of the soft soil layer is 6.46–18.5 m; in the segment from Magang Avenue to Zhongxinhe Road, the soft soil layer is dominated by continuously distributed silty soil and silt. The thickness of the soft soil layer is 5.57–11.62 m.

B. Experimental Data and Processing

A total of 23 TerraSAR-*X*-band Stripmap descent images covering the test area were collected, with a spatial resolution of 3 m (3.30 m along azimuth, 2.64 m along the range, and the average incident angle of 26.4°). Those images were from January 1, 2015 to January 18, 2017. The multilook ratio along the range and azimuth directions was set as 1:1 to ensure the best resolution of the test highway. During the SBAS processing, the spatial–temporal thresholds of the interferometric combination were set as 130 m and 300 days empirically. The specific spatial–temporal baselines were illustrated in Fig. 6 and the SAR sensor parameters are given in Table I. The shuttle radar topography mission digital elevation model (DEM) data with a spatial resolution of 30 m was utilized to remove the topographic phase. Gaussian filter was used to filter the interferometric phase to suppress the noise. After the smoothed and filtered differential interferograms were generated, the orbital error was removed by the polynomial fitting method. After a phase unwrapping for the wrapped deformation phase with the minimum cost flow algorithm, a total of 134 unwrapped interferograms were generated [40].

During processing, high-coherence candidates were selected based on a coherence threshold of 0.8. To ensure that the most coherence points were distributed over the highway among the 134 total interferometric pairs, we selected the interferograms carefully and deleted those with bad coherence and fewer points along the route [41]. Consequently, only 40 high-quality pairs with densely distributed coherence pixels over the highway region were selected. The subsequent experiments, including
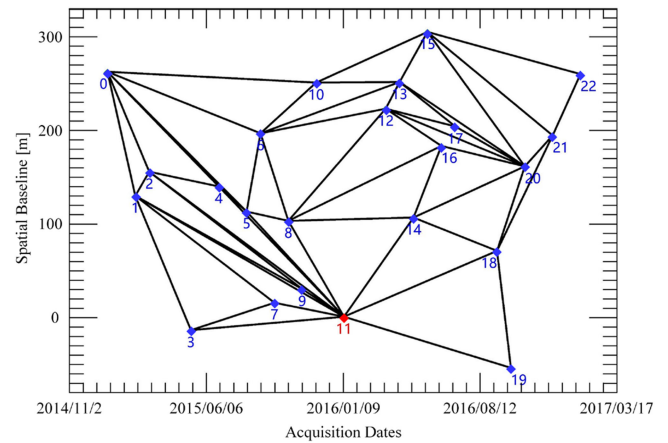

Fig. 6. Spatial–temporal baselines of each interferometric pair (*X*-axis defines the acquisition dates of SAR images; *Y*-axis defines the perpendicular baselines; the red rhombus represents the supermaster image).

TABLE I
LIST OF THE INTERFEROMETRIC PAIRS AND THEIR PARAMETERS WITH IMAGE NUMBER 11 AS THE MASTER (ORBIT NO. 119)

Image No.	Acquisition Date (yyyy/mm/dd)	Normal Baseline (m)	Temporal Baseline (Days)
0	2015/01/01	261.34	-374
1	2015/02/14	128.54	-330
2	2015/03/08	154.36	-308
3	2015/05/13	-14.42	-242
4	2015/06/26	138.72	-198
5	2015/08/09	112.02	-154
6	2015/08/31	195.53	-132
7	2015/09/22	14.18	-110
8	2015/10/14	102.02	-88
9	2015/11/05	29.16	-66
10	2015/11/27	249.74	-44
11	2016/01/10	0	0
12	2016/03/16	221.17	66
13	2016/04/07	250.27	88
14	2016/04/29	105.41	110
15	2016/05/21	303.80	132
16	2016/06/12	182.00	154
17	2016/07/04	203.15	176
18	2016/09/08	69.64	242
19	2016/09/30	-54.80	264
20	2016/10/22	159.64	286
21	2016/12/05	192.98	330
22	2017/01/18	258.26	374

time-series deformation model, model parameter estimation, and deformation sequences retrieving, were carried out with MATLAB programs. To improve the quality of the high-coherence points, the triple threshold method, which considers the amplitude dispersion index, the coherence coefficient, and the intensity combinedly, was used to extract the high-coherence points in the test area. The thresholds of the three indices were set as 0.26, 0.8, and 0.6, respectively. Finally, 2567 high-coherence points were identified [33].

According to (5), for each high-coherence point, GARN was used to estimate the following unknown parameters: maximum subsidence W_0, Poisson shape parameters a and b, linear velocity v, and elevation corrections Δh. According to previous studies on the soft soil of the test highway, the initial range
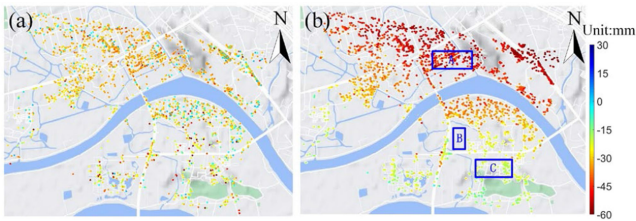
Fig. 7. Comparison of the estimated maximum deformation W_0. (a) GA. (b) GARN.

Fig. 8. Comparison of the estimated linear velocity v. (a) GA. (b) GARN.

Fig. 9. Comparison of the estimated elevation corrections Δh. (a) GA. (b) GARN.

Fig. 10. Comparison of the estimated Poisson shape parameter a. (a) GA. (b) GARN.

Fig. 11. Comparison of the estimated Poisson shape parameter b. (a) GA. (b) GARN.

of individual genes was set as follows: W_0 was set within the interval of $[-0.12, 0.08]$ m, a within the interval of $[0, 150]$, b within $[0, 15]$, v within $[-0.06, 0.04]$ m, and Δh within $[-15, 15]$ m [24], [45], [47]–[49]. During the GA searching, the upper limit of the genetic population was set as 900 generations, with 10 000 individuals in each population. The crossover probability and mutation probability were set as 0.92 and 0.08, respectively. The crossover model was a two-point crossover, and a Gaussian function was selected as the mutation function. The termination condition for the program iterations was the minimization of the average fitness function value, which indicated a stable fitness value. Finally, the individual gene of the population satisfying the minimum fitness function value was obtained, which was taken as the initial input value for the subsequent RN secondary optimization. After the GARN processing, the final estimations for all the model parameters have been obtained. Substituting the estimated parameters into (5), the LP-deformation component at each high-coherence point can be obtained. Since the atmospheric delay belongs to high frequency in time and low frequency in space, whereas the noise phase belongs to a high frequency, the HP-deformation component in the residual phase can be recovered through temporal HP filtering and spatial LP filtering [21]. Finally, through the sum of the HP deformation and LP deformation, the time-series deformation results over all the high-coherence points can be obtained.

C. Experimental Results and Discussions

During the GA searching process, the number of iterative searching times for the global optimal model parameters was set to 10 000 times. However, nonconvergency still existed on large amount of points at the end of the iteration, which led to unavoidable random errors in the final exported solutions. As introduced in Section II, with the GA-generated solutions as the initial values, the RN iteration algorithm was used as a secondary optimization for the rough GA-generated estimations. The final estimations for each high-coherence point were generated after a stable 20 times iterative calculation at most. The comparison for the estimated maximum subsidence W_0, Poisson shape parameters a and b, linear velocity v, and elevation corrections Δh between GA and GARN is shown in Figs. 7–11, respectively. Since parameters a and b have no obvious rules in their spatiotemporal distributions, it is not obvious to demonstrate the optimization effect by using GARN in Figs. 10 and 11. However, it can be seen from Figs. 7–11 that the GA-generated results have more obvious noisy points induced by the random
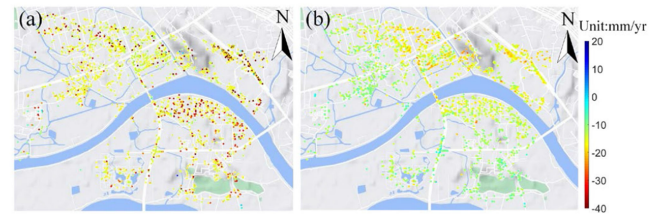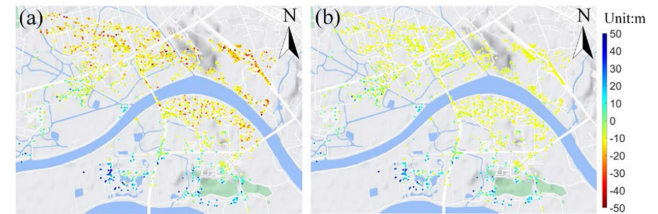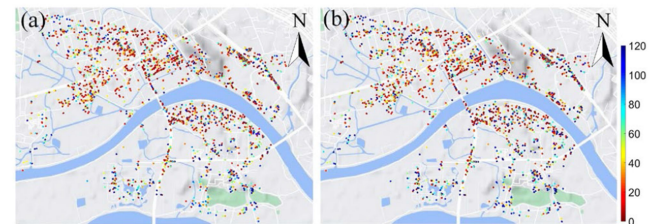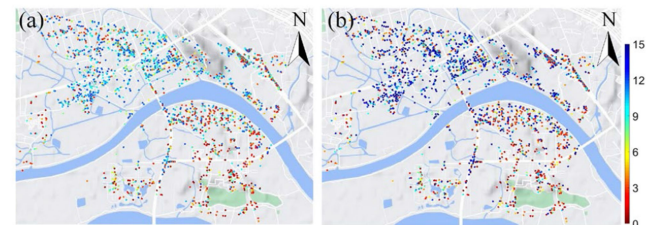
error contained in the GA nonconvergency searching, whereas the GARN-generated estimations seem smoother. The GA estimated parameters for some points with the fitness function not satisfied may be outputted as the final estimation. This is the suggested reason why the GA-generated results contain more noise for the five parameters.

For the Poisson curve, W_0 mainly affects the maximum subsidence position, while a and b mainly influence the curvature distribution along the temporal axis. The higher the a is, the longer a point will remain stable before sinking, and accordingly, the longer it will last up to the maximum subsidence, whereas the higher the value of b, the faster the ground points will subside. As can be seen from Fig. 7 that the theoretical maximum subsidence value of all the points in the area mainly distribute within the interval of $[-60, -10]$ mm. According to our *in situ* investigation,
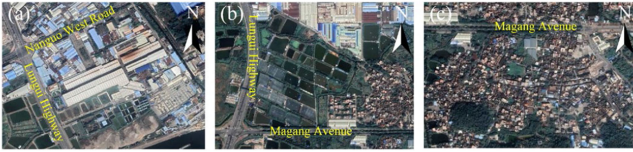
Fig. 12. Enlarged images for (a) area A, (b) area B, and (c) area C in Fig. 7(a).

for the areas marked within the blue frames in Fig. 7(b) (with the corresponding enlarged view, as shown in Fig. 12), we found that villages, ponds, and industrial areas dominate area A north Magang Avenue around the upper stretch of the highway, and densely distributed ponds [see the dark rectangles in Fig. 12(b)] were mainly located in area B. As the geological characteristic is shown in Fig. 5(d), the soil along the upper stretch of the highway was mainly composed of mucky clay and silt. Besides, the water system around this stretch was well developed, resulting in which the ground subsidence was more obvious with the maximum subsidence up to 85 mm in area A and 66 mm in area B, respectively. In contrast, in the southern part (the bottom part below Magang Avenue) of the whole area, urban buildings, such as banks, office buildings, and residential areas, were densely distributed [marked as area C in Fig. 7(b)]. Consequently, as the content of silty clay contained in the soil around the lower stretch of the highway was relatively much lower, the settlement was much weaker with the maximum subsidence of only 32 mm. Figs. 10 and 11 show the two Poisson shape parameters a and b, respectively. From the perspective of the spatial distribution, no obvious tendency of the color distribution can be found in both a and b for all the high-coherence points, with their values distributed within the range of [0, 120] and [0, 15], respectively. The reason for the noisy distribution phenomenon is related to the large deviations of the Poisson shape parameters magnitudes between different points. The obtained linear velocities and elevation corrections are shown in Figs. 8 and 9, respectively. It can be generally seen that the values of v are mainly distributed from −20 to 0 mm/yr, whereas from −10 to 10 m for Δh, respectively.

Fig. 13 shows the total time-series settlement results obtained based on the advanced time-series InSAR approach. Figs. 14 and 15 are the enlarged time-series deformation results near the two benchmarks BM1 and BM2, as marked in Fig. 13 (which will be discussed in Section IV-D). From the spatial characteristics of the color distribution, we can see that Magang Avenue is still the obvious dividing line in the images (with a dark red color in the upper area) and that the maximum subsidence was 85 mm (on January 18, 2017). The deformation was significantly weaker in the bottom part (generally blue–green), with maximum subsidence of only 45 mm. As shown in Fig. 5(d), with densely distributed ponds around the upper stretch of the highway, mucky clay and silt dominated the geological content of the clay. Accordingly, the soft soil layer of the upper segment was relatively thicker, with a thickness of 6.64–18.5 m. Moreover, the water system around this stretch was well developed and, thus, the ground subsidence was more obvious. Comparatively, the areas south of Magang avenue in the image were mainly urban districts, where the silt content in the soil of the road

foundation was lower, with mealy sand and silty clay as the dominant geotechnical content. Compared with the upper stretch of the highway, the average thickness of the soft soil layer was only 5.57–11.62 m. Furthermore, an advanced drainage system was equipped in the urban areas, thus with a lower water discharge flow under the surface. Consequently, the settlement of the southern part was much weaker.

From the temporal color variation in Fig. 13, it can be found that the deformation was rapid from the initial time to May 13, 2015, with the subsidence velocity decreasing slowly. However, from January 10, 2016 to July 4, 2016, the deformation showed relatively stable performance. Distinct jumps were detected for three periods in this area (May 13 to August 31, 2015; November 27, 2015 to January 10, 2016; and July 4, 2016 to September 8, 2016), with a maximum recovery of 18 mm (which will be discussed later in detail).

In order to further investigate the temporal characteristics of the surface deformation, two feature points (marked as D and E in Fig. 13, the locations on the optical images are shown in Fig. 16) were extracted. Point D is located at the intersection of Junma Road and Junma Three Ways and E at the intersection of Lungui Highway and Magang avenue. The results generated by the pure linear velocity model were used as a comparison, and the corresponding two groups of deformation sequences of the two points were shown in Figs. 17 and 18, respectively. It can be clearly seen that, compared with the red polyline, the blue polyline seems more reasonable in representing the actual deformation of the soft soil, indicating that the solution generated by GARN is more accurate than using a single GA. The observed total surface deformation derived by the Poisson curve showed generally fast subsidence at the beginning, followed by a slower trend and finally reaching a stable state at both the two points. Comparatively, as shown in Fig. 17, the Poisson curve-generated subsidence was quite obvious (with accumulated subsidence to 49 mm) at point D, whereas the maximum subsidence generated by the linear velocity model was only 35 mm. The difference between the two groups of results was mainly related to the large nonlinear component of the deformation obtained at point D. The nonlinear deformation component that cannot be fitted by the linear velocity model was contained and modeled in the Poisson curve function, thus was weaker than the Poisson curve-generated results. This indicates that a majority of the nonlinear deformation may not be reflected in the residual phase of the linear velocity model when a substantial real nonlinear deformation has occurred. Therefore, the obtained nonlinear deformation result, isolated from the residual phase of the linear model, may have a large deviation from the real value. As shown in Fig. 18, due to the relatively low residual phase component for the linear velocity model, the subsidence trend of the two models at point E was more consistent from January 2015 to January 2017, with the relatively lower deviation of 10 mm (the maximum subsidence of the linear model of 27 mm and that of the Poisson curve of 35 mm).

According to the article presented in [46], we also conducted an experiment based on the traditional cubic polynomial model. The temporal deformation time series at the two feature points is extracted and demonstrated as the orange polyline in Figs. 17
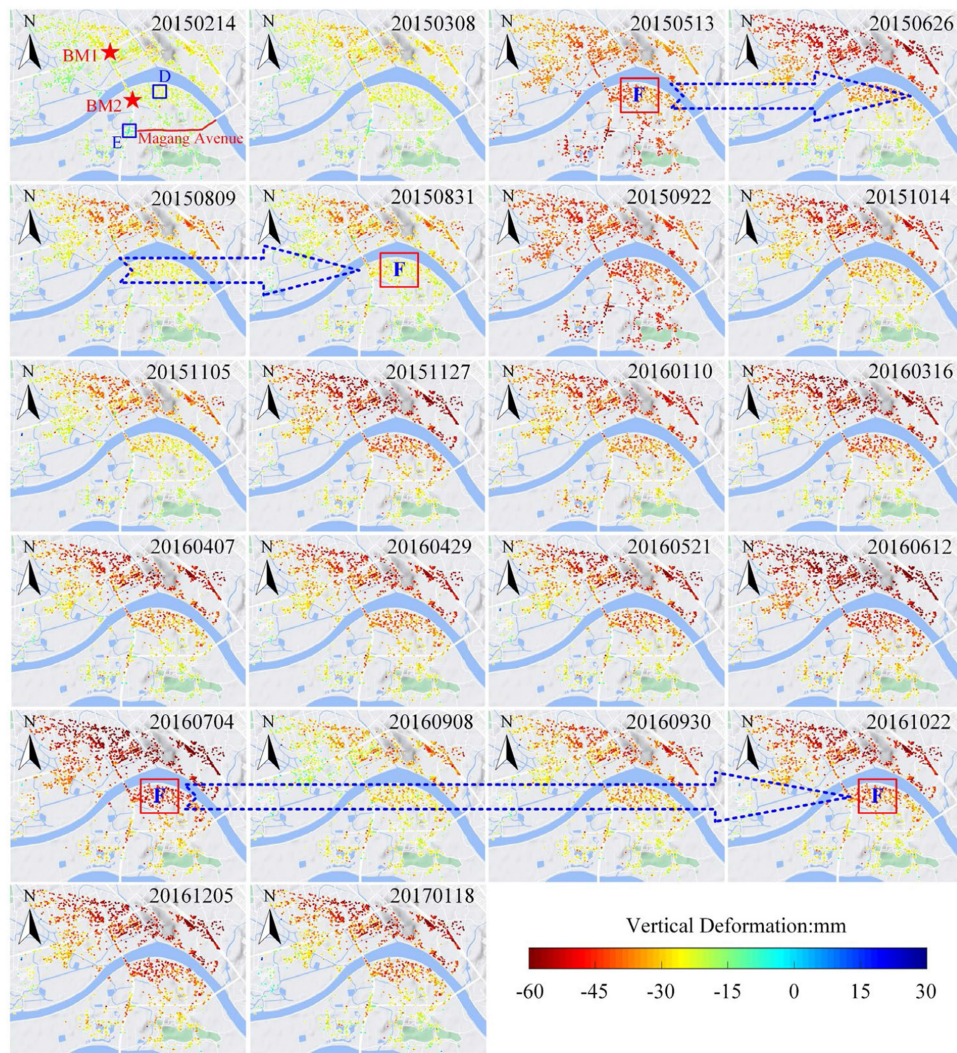
Fig. 13. Obtained time-series deformation (with reference to January 1, 2015).

and 18. As they both display, the total temporal variations for both the two points reveal a stable deformation speed at the beginning (from January 2015 to August 2015) and followed with a gradually increasing subsiding trend (from September 2015 to January 2017), with the deformation rate increased significantly. This is considerably different from the reality of the soft clay, which is suggested following a gradually decreasing characteristic of subsidence and reaching a final stable state. The reason for this wrong result is recommended related to the cubic polynomial model itself. When the actual temporal variations of the displacement described by the cubic polynomial model do not follow the characteristics of the function, the estimated deformation results may be incorrect, although it shows advantages in empirical mathematical functional modeling with spatial approximation.

The three uplift periods mentioned above were detected for both the two points (marked with pink arrows in the figures), which were hidden in the results generated by the linear velocity model at point D and point E. Those patterns are suggested related to the geological properties of soft soil, the time of

highway construction, and the climatic and hydrological conditions over this area with high natural water content and high compressibility. Due to the influence of constant external load, the space between soil particles is compressed, and the deformation from the initial time to June 2015 was characterized by a high subsidence rate. With the pass of time, when the natural compression of the soil reaches its limit and the porosity ratio drops to its minimum, the deformation caused by the external load and water-bearing exfiltration in the soft soil is over. Therefore, the subsequent deformation was mainly affected by external environmental factors. As shown in Figs. 17 and 18, according to Foshan precipitation data provided by the meteorological agency [42], in 2015, the annual rainfall was 5770.8 mm, and the uneven spatial–temporal distribution of the precipitation may reach up to 1684.8 mm. Compared with April, the total rainfall increased by 1497.8 mm (see the first pink arrow in Fig. 16), accounting for about 30% of 4265.7 mm from May to September, almost four times that of the other months. With the increase of rainfall, the foundation of the ground surface was influenced by the precipitation and the surrounding water
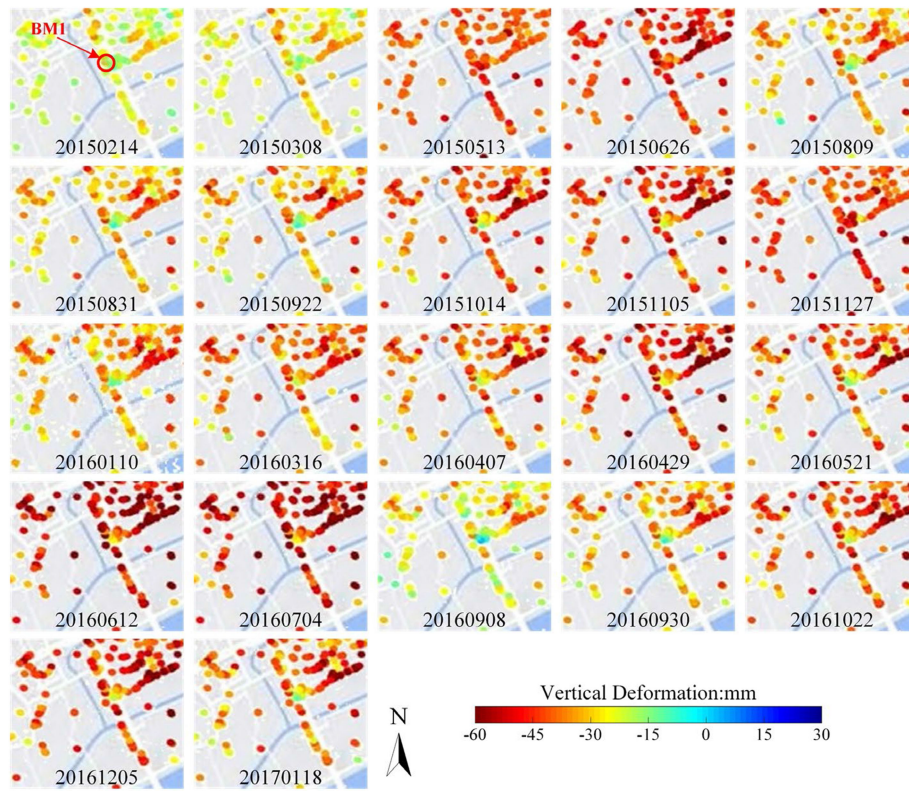
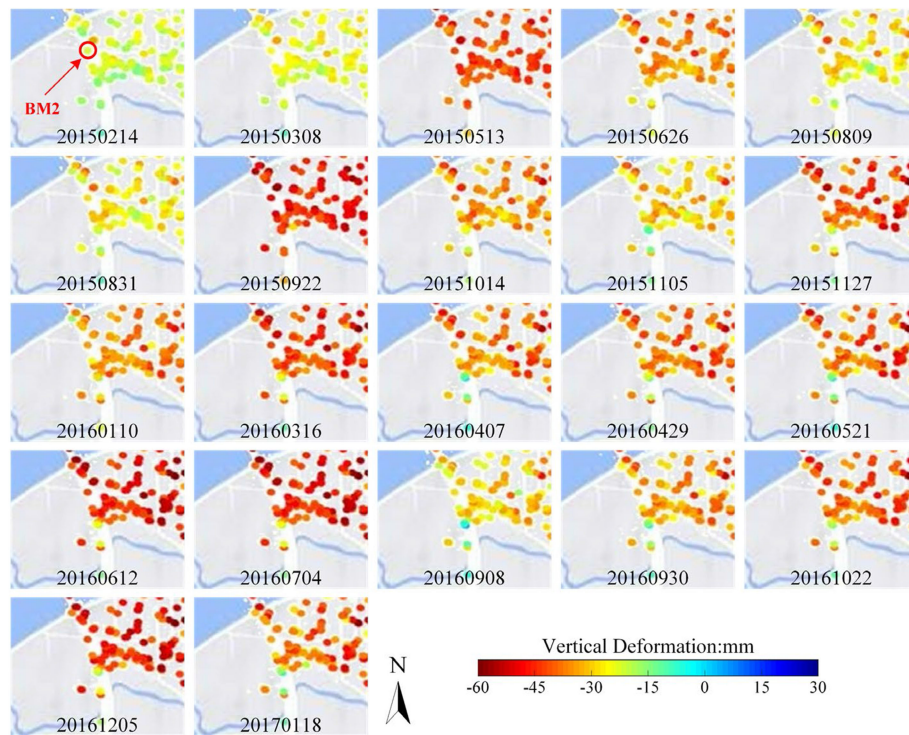Fig. 14. Enlarged deformation sequences around BM1 in Fig. 13.

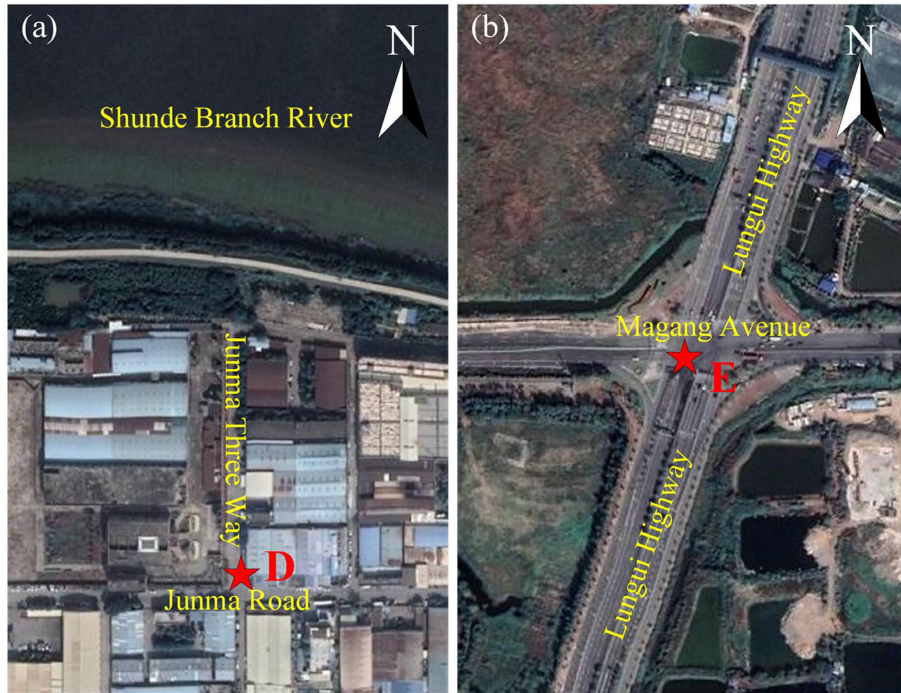Fig. 15. Enlarged deformation sequences around BM2.

Fig. 16. Enlarged images of the feature points (with optical images as background). (a) Point D is located at the intersection of Junma Road and Junma three ways. (b) Point E is located at the intersection of Lungui Highway and Magang Avenue.
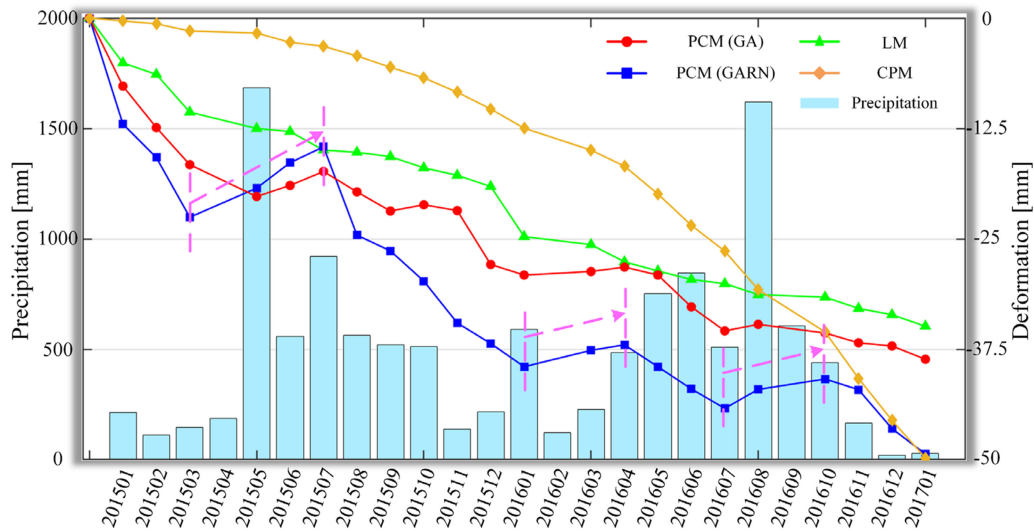

Fig. 17. Time-series deformation at feature point D (with reference to January 1, 2015; *X*-axis represents the dates of SAR acquisitions; *Y*-axis represents the InSAR-generated deformation; PCM: Poisson curve model; LM: linear model; CPM: cubic polynomial model).

supplies, leading to an 8 mm's recovery from May 13, 2015 to August 31, 2015, for point D. Similar temporal variations could be found at rest two periods in which uplifts with a recovery of 3 and 4 mm occurred during the periods from March 16, 2016 to April 29, 2016, and from July 4, 2016 to September 30, 2016, respectively (marked as pink arrows in Figs. 17 and 18). Similarly, the maximum settlement generated by the Poisson curve was accumulated to 34 mm at point E with three periods of recoveries of 4, 3, and 3 mm, respectively (see Fig. 18). To verify the influence of the precipitation on the obtained

deformation, we calculate the correlation coefficients between the deformation sequences and precipitation data series at points D and E, which are estimated as 0.62 and 0.51, respectively. The results imply that the deformation at both two points is highly correlated with the precipitation, which quantitively supports the rationality of the above discussion.

To intuitively show the detailed temporal variations for the subsidence compared with the results generated by the linear velocity model, the deformation over area F (marked in Fig. 13) was extracted and enlarged, which is shown in Fig. 19.
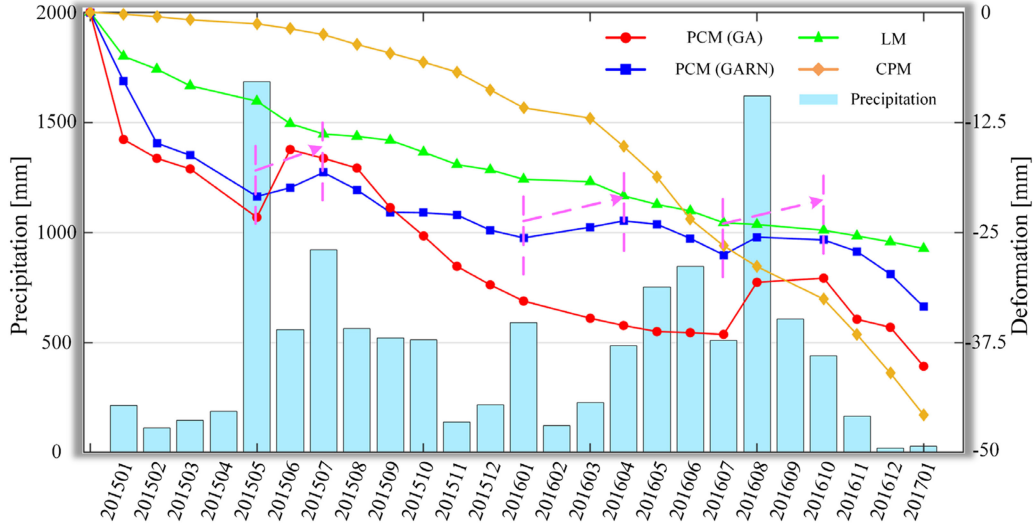
Fig. 18.   Time-series deformation at feature point E (with reference to January 1, 2015; *X*-axis represents the dates of SAR acquisitions; *Y*-axis represents the InSAR-generated deformation; PCM: Poisson curve model; LM: linear model; CPM: cubic polynomial model).
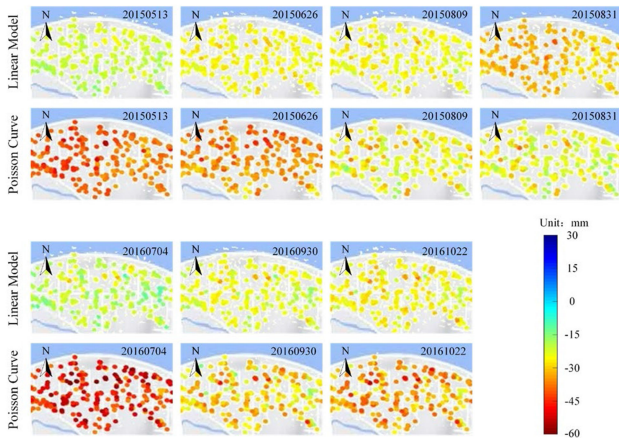

Fig. 19.   Enlarged deformations over area F with a comparison to that of the linear velocity model.

From the spatial distribution of colors in the figure, the time-series deformation derived by the Poisson curve has a relatively higher variation compared with that obtained with the linear model, indicating that the Poisson model can better extract the nonlinear deformation component and describe the uplift phenomenon of the soft soil in the study area. Combining Figs. 17 and 18, we can see that the recoveries related to the precipitation (marked with blue arrows in Fig. 13; from May 2015 to August 2015 and from July 2016 to October 2016), which were hidden in the linear velocity results, could be better detected by the proposed method.

D. Accuracy Validation

The degree of ill-condition or singularity for the matrix G_k in (7) can influence the estimation precision for the unknown parameters significantly. To test the effectiveness of GARN during the iterative process, 2567 high-coherence points were extracted
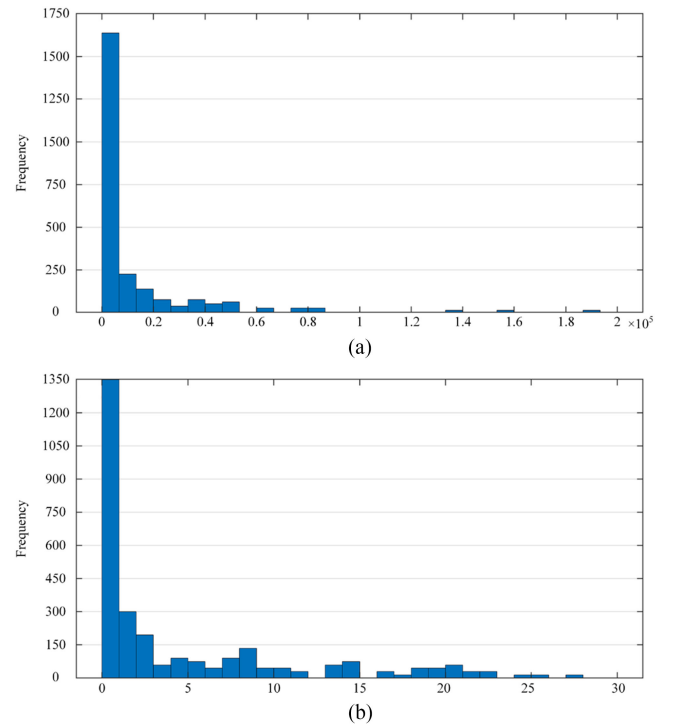

Fig. 20.   Statistical curves of condition numbers for the two methods (*X*-axis represents the ranges of the condition numbers and *Y*-axis represents the frequency of the points). (a) Newton iterative algorithm. (b) RN iterative algorithm.

to test the degree of ill-condition for G_k. As introduced in [43], the condition number for a matrix can reflect the ill-condition degree effectively. If the condition number is high, the matrix is ill; if the condition number is low (close to 1), the matrix can be treated as healthy. Consequently, the condition number at each coherence point before (for singular G_k) and after (for $G_k + \alpha^k I$ instead) regularization and the statistic curves over all the points are shown in Fig. 20. As can be seen from
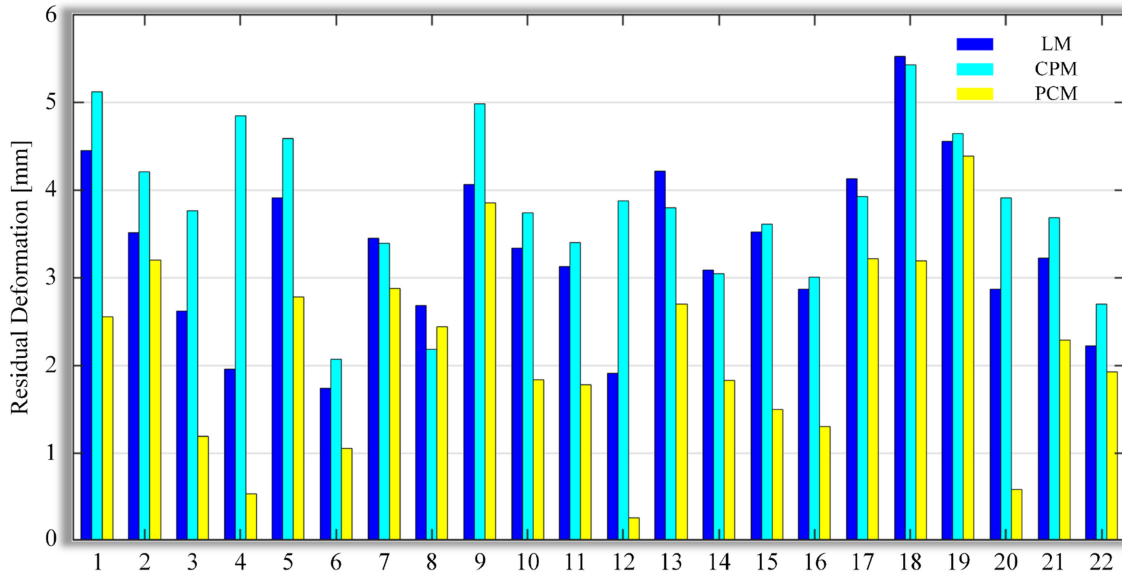
Fig. 21.   STDs of HP-deformation comparison of 22 SAR images (LM: linear model; CPM: cubic polynomial model; PCM: Poisson curve model).
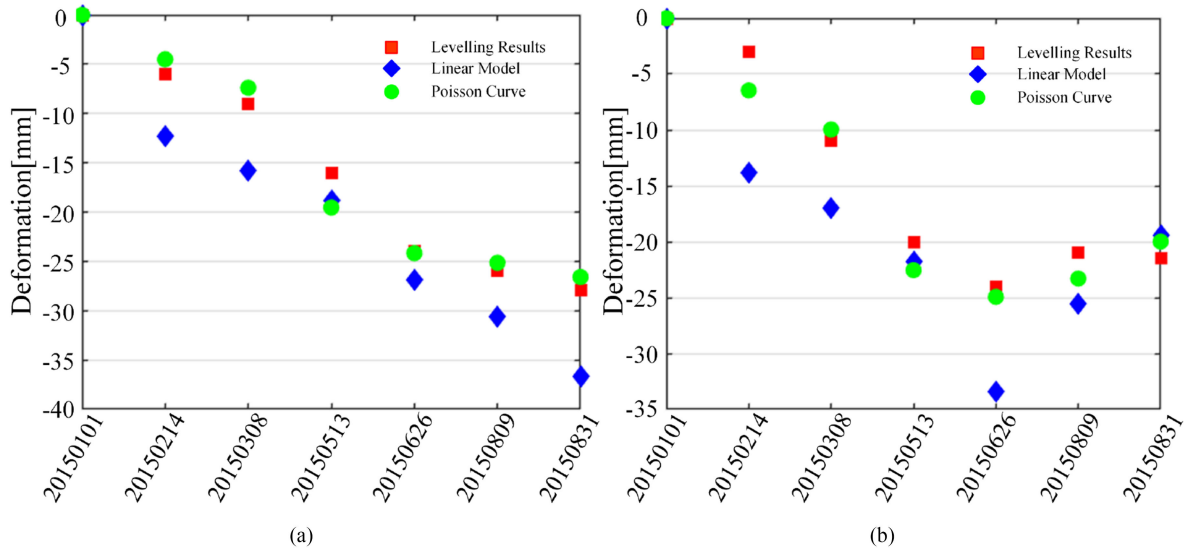

Fig. 22.   Time-series deformation results compared with leveling measurements on benchmarks. (a) BM1 in Fig. 9. (b) BM2.

the figure that the points with condition numbers higher than 600 account for 90.3% (2319) of the ordinary Newton iterative algorithm, while points with condition numbers lower than 5 after GARN processing account for 78.7% (2021). Obviously, the RN iterative processing can improve the ill-condition of the iterative matrix G_k.

According to the article presented in [44], the magnitude of the HP-deformation component can reflect the degree of fitting accuracy of the model. The smaller the HP-deformation component is, the higher the modeling accuracy is. The HP deformation of each interferogram obtained through the Poisson curve combined with GARN was compared with that of the linear velocity model. Fig. 21 shows a comparison of the HP-deformation overall high-coherence points for each

interferogram. As shown in Fig. 21, all the HP deformations were lower than 6 mm. For all the interferograms, the HP deformation generated by the Poisson curve was ±2.4 mm less than that of the linear model, indicating that the Poisson curve is more suitable for the time-series deformation in the test area. The standard deviations (STDs) of the HP deformation were ±3.4 mm of the linear model and ±4.0 mm of the cubic polynomial. The accuracy of our method was with an improvement of 29.4% compared with the linear model.

In addition, we collected the leveling measurements at two leveling points in the test highway. The locations of the two Benchmarks are shown in Fig. 13 (BM1 and BM2), which are mainly distributed near the Anlite Bridge. The temporal span of the leveling measurements was from June 2014 to August

TABLE II
RMSE COMPARISON OF THE BENCHMARKS IN FIG. 9

	BM1	BM2	RMSE
Linear Model	±6.8	±5.8	±6.2
Poisson Curve	±2.2	±1.8	±2.0

Unit: mm.

2015. To carry out the accurate comparison, we transferred the generated LOS deformation into vertical displacement according to the equation $S_{\text{LOS}} = S_v \cos\theta$ and extracted the six dates of the measurement data that spanned the same period with our SAR acquisition dates. The total reference point of leveling and all the SBAS processing methods were the same pixel, which was selected according to our *in situ* investigation and registered deformation material collection. The comparison results are shown in Fig. 22. As shown in the figure, the blue diamond block represents the deformation results of the linear velocity model and the green circle represents the results of the Poisson curve model combined with GARN. It can be seen from the comparison results that the Poisson curve model shows better consistency with the leveling measurements. Table II presents the quantitative comparison results of the RMSE on the benchmarks. According to our calculation, the RMSE of the linear model was ±6.2 mm, while the Poisson curve with the GARN algorithm was ±2.0 mm, with an improvement of about 67%.

V. CONCLUSION

In this article, an advanced InSAR approach for soft clay highway deformation monitoring was proposed. In the approach, both the InSAR deformation model and the parameter estimation algorithm were improved. The improved InSAR deformation model was based on the Poisson Curve, which considers the characteristics of the temporal physical deformation evolution of the soft clay. The improved algorithm for the unknown parameter estimation is based on a GARN algorithm, which can estimate the model parameters considering both the advantages of the GA and the RN iterative algorithm combinedly. The results of the simulation showed that under certain noise levels, the GARN-generated parameters (maximum subsidence W_0, Poisson shape parameters a and b, linear velocity v, and elevation corrections Δh) showed better coincidence with the true values compared with that of singular GA. In the real data experiment, a sketch of Lungui Highway in Foshan, Guangdong Province, was selected as the test area. With the use of 23 TerraSAR-*X*-band high-resolution images, the time-series deformation from January 1, 2015 to January 18, 2017 was retrieved. The experimental results showed that the total derived surface deformation was generally fast subsidence at the beginning and then a slower trend reaching a stable state, with the maximum accumulative subsidence of 85 mm. Three uplifts, which were suggested related to the increment of precipitation, were detected with the maximum recovery of 18 mm.

To evaluate the accuracy of the obtained results generated by our method, the STDs of HP deformation were calculated, and the results showed that the STDs generated by our method were reduced by 23% compared with the traditional SBAS-InSAR based on the linear velocity model. The external accuracy for the highway was evaluated by the *in situ* leveling measurements, and the average RMSE of our results was estimated as ±2.0 mm, with an improvement of 67% compared with the traditional SBAS-InSAR-generated results, indicating the greater reliability and feasibility of our methods over the soft clay area.

REFERENCES

[1] X. Xue, L.-L. Song, L. Jia, Y. Le, and H. Ge, "New prediction method for post-construction settlement of soft-soil roadbed of expressway," *Chin. J. Geotech. Eng.*, vol. 33, pp. 125–130, Aug. 2011.

[2] J. Xia, G.-L. Huang, and S.-B. Yan, "Behaviour and engineering implications of recent floodplain soft soil along lower reaches of the Yangtze River in Western Nanjing, China," *Eng. Geol.*, vol. 87, no. 1/2, pp. 48–59, Sep. 2006, doi: 10.1016/j.enggeo.2006.05.006.

[3] M. H. Zhao, Y. Liu, and W. G. Cao, "The developing regularity and forecasting of settlement in soft clay roadbed," *J. Central South Univ. (Sci. Technol.)*, vol. 35, no. 1, pp. 157–161. Feb. 2004.

[4] D. Ge, Y. Wang, X. Guo, Y. Wang, and Y. Xia, "Land subsidence investigation along railway using permanent scatterers SAR interferometry," in *Proc. IEEE Int. Geosci. Remote Sens. Symp.*, 2008, pp. 1235–1238, doi: 10.1109/IGARSS.2008.4779225.

[5] M. Amighpey and S. Arabi, "Studying land subsidence in Yazd Province, Iran, by integration of InSAR and levelling measurements," *Remote Sens. Appl., Soc. Environ.*, vol. 4, pp. 1–8, Oct. 2016, doi: 10.1016/j.rsase.2016.04.001.

[6] J. W. Chen, "Present and prospect of InSAR-GPS integration for research of land subsidence," *Sci. Surv. Map.*, vol. 28, no. 4, pp. 69–71. Dec. 2003.

[7] Z. W. Li, X. L. Ding, and G. X. Liu, "Modeling atmospheric effects on InSAR with meteorological and continuous GPS observations: Algorithms and some test results," *J. Atmos. Sol.-Terr. Phys.*, vol. 66, no. 11, pp. 907–917, Jul. 2004, doi: 10.1016/j.jastp.2004.02.006.

[8] H. A. Zebker and J. Villasenor, "Decorrelation in interferometric radar echoes," *IEEE Trans. Geosci. Remote Sens.*, vol. 30, no. 5, pp. 950–959. Sep. 1992.

[9] J. C. Mura *et al.*, "Monitoring the vulnerability of the dam and dikes in Germano iron mining area after the collapse of the tailings dam of Fundão (Mariana-MG, Brazil) using DInSAR techniques with TerraSAR-X data," *Remote Sens.*, vol. 10, no. 10, Sep. 2018, Art. no. 1507, doi: 10.3390/rs10101507.

[10] X. Hu, T. Oommen, Z. Lu, T. Wang, and J.-W. Kim, "Consolidation settlement of salt lake county tailings impoundment revealed by time-series InSAR observations from multiple radar satellites," *Remote Sens. Environ.*, vol. 202, pp. 199–209, Dec. 2017, doi: 10.1016/j.rse.2017.05.023.

[11] A. Ferretti, C. Prati, and F. Rocca, "Permanent scatterers in SAR interferometry," *IEEE Trans. Geosci. Remote Sens.*, vol. 39, no. 1, pp. 8–20, Jan. 2001.

[12] P. Berardino, G. Fornaro, R. Lanari, and E. Sansosti, "A new algorithm for surface deformation monitoring based on small baseline differential SAR interferograms," *IEEE Trans. Geosci. Remote Sens.*, vol. 40, no. 11, pp. 2375–2383, Nov. 2002.

[13] J. Zhu, Z. Li, and J. Hu, "Research progress and methods of InSAR for deformation monitoring," *Acta Geodaetica et Cartographica Sinica*, vol. 46, no. 10, pp. 1717–1733, Oct. 2017.

[14] X. Qin, M. Yang, H. Wang, T. Yang, J. Lin, and M. Liao, "Application of high-resolution PS-InSAR in deformation characteristics probe of urban rail transit," *Acta Geodaetica et Cartographica Sinica*, vol. 45, pp. 713–721, 2016.

[15] H. Lin, P. Ma, and W. Wang, "Urban infrastructure health monitoring with spaceborne multi-temporal synthetic aperture radar interferometry," *Acta Geodaetica et Cartographica Sinica*, vol. 46, no. 10, pp. 1421–1433, Oct. 2017.

[16] H. Lin, F. Chen, L. Jiang, Q. Zhao, and S. Cheng, "Preliminary research on large-scale man-made linear features deformation monitoring using multi-baseline differential SAR interferometry," *J. Geo-Inf. Sci.*, vol. 12, no. 5, pp. 718–725, Oct. 2010.

[17] D. Tapete, S. Morelli, R. Fanti, and N. Casagli, "Localising deformation along the elevation of linear structures: An experiment with space-borne InSAR and RTK GPS on the roman aqueducts in Rome, Italy," *Appl. Geogr.*, vol. 58, pp. 65–83, Mar. 2015, doi: 10.1016/j.apgeog.2015.01.009.

[18] M. Lazecky, D. Perissin, M. Bakon, J. M. de Sousa, I. Hlavacova, and N. Real, "Potential of satellite InSAR techniques for monitoring of bridge deformations," in *Proc. Joint Urban Remote Sens. Event*, 2015, pp. 1–4, doi: 10.1109/JURSE.2015.7120506.

[19] S. Dong, S. Samsonov, H. Yin, S. Ye, and Y. Cao, "Time-series analysis of subsidence associated with rapid urbanization in Shanghai, China measured with SBAS InSAR method," *Environ. Earth Sci.*, vol. 72, pp. 677–691, Aug. 2014, doi: 10.1007/s12665-013-2990-y.

[20] B. Yu *et al.*, "Monitoring subsidence rates along road network by persistent scatterer SAR interferometry with high-resolution TerraSAR-X imagery," *J. Modern Transport.*, vol. 21, pp. 236–246, Dec. 2013, doi: 10.1007/s40534-013-0030-y.

[21] M. S. Liao and T. Wang, *Time Series Insar Technology and Application*. Beijing, China: Science Press, 2014, pp. 83–86.

[22] S.-S. Li, Z. Li, H. Jun, Q. Sun, and X.-Y. Yu, "Investigation of the seasonal oscillation of the permafrost over Qinghai-Tibet plateau with SBAS-InSAR algorithm," *Chin. J. Geophy.*, vol. 56, no. 5, pp. 1476–1486, May 2013.

[23] Y. H. Zhang, H. Wu, and G. Sun, "Deformation model of time series interferometric SAR techniques," *Acta Geodaetica et Cartographica Sinica*, vol. 41, no. 6, pp. 864–869, Dec. 2012.

[24] Z. Zhu and L. Zhou, "Application of logistic model in settlement prediction during complete process of embankment construction," *Chin. J. Geotech. Eng.*, vol. 31, no. 6, pp. 965–969, Jun. 2009.

[25] M.-H. Zhao, Y. Liu, and W.-G. Cao, "Study on variable-weight combination forecasting method of S-type curves for soft clay embankment settlement," *Rock Soil Mech.*, vol. 26, no. 9, pp. 1443–1447, Sep. 2005.

[26] G. X. Mei, J. M. Zai, Z. Z. Yin, W. B. Zhao, and J. Yin, "Proof of st curve appearing S shape based on one-dimensional consolidation theory," *Rock Soil Mech.*, vol. 25, no. 1, pp. 20–22, Jan. 2004.

[27] G. X. Mei, J. M. Zai, W. B. Zhao, and Z. T. Liu, "Proof of St curve appearing S shape and its application," *J. Nanjing Univ. Technol.*, vol. 25, no. 4, pp. 6–9, Jul. 2003.

[28] B. M. Kampes and R. F. Hanssen, "Ambiguity resolution for permanent scatterer interferometry," *IEEE Trans. Geosci. Remote Sens.*, vol. 42, no. 11, pp. 2446–2453, Nov. 2004.

[29] X. Xing, H.-C. Chang, L. Chen, J. Zhang, Y. Zhihui, and Z. Shi, "Radar interferometry time series to investigate deformation of soft clay subgrade settlement—A case study of Lungui Highway, China," *Remote Sens.*, vol. 11, no. 4, Feb. 2019, Art. no. 429, doi: 10.3390/rs11040429.

[30] X. Z. Wang, *Theory and Application of Parameter Estimation for Nonlinear Models*. Wuhan, China: Wuhan Univ. Press, 2002.

[31] L. M. Tang, "Research on the Ill-posed and solving methods of nonlinear least squares problem," *Acta Geodaetica et Cartographica Sinica*, vol. 41, no. 4, Aug. 2012, Art. no. 630.

[32] S. Usai, *A New Approach for Long-Term Monitoring of Deformations by Differential SAR Interferometry*. Delft, The Netherlands: Delft Univ. Press, 2001.

[33] X.-M. Xing *et al.*, "Detecting the regional linear subsidence based on CRInSAR and PSInSAR integration," *Chin. J. Geophys.*, vol. 54, no. 5, pp. 1193–1204, May 2011.

[34] T. R. Lauknes, H. A. Zebker, and Y. Larsen, "InSAR deformation time series using an L_1-norm small-baseline approach," *IEEE Trans. Geosci. Remote Sens.*, vol. 49, no. 1, pp. 536–546, Jan. 2011.

[35] Z. F. Yang, H. W. Yi, J. J. Zhu, Z. W. Li, M. J. Sun, and Q. Liu, "Spatiotemporal evolution law analysis of whole mining subsidence basin based on InSAR-derived time-series deformation," *Trans. Nonferrous Metals Soc. China*, vol. 26, no. 7, pp. 1515–1522, Jul. 2016.

[36] Z. Yang, Z. Li, J. Zhu, H. Yi, H. Jun, and G. Feng, "Deriving dynamic subsidence of coal mining areas using InSAR and logistic model," *Remote Sens.*, vol. 9, no. 2, Feb. 2017, Art. no. 125, doi: 10.3390/rs9020125.

[37] Y. G. Tian, *Study on Genetic Algorithm for Nonlinear Least Squares Estimation*. Wuhan, China: Wuhan Univ. Press, 2003.

[38] L. M. Tang and J. J. Zhu, "Regularized newton iterative algorithm for poisson model of soft clay embankment settlement," *Geomat. Inf. Sci. Wuhan Univ.*, vol. 38, no. 1, pp. 69–73, Jan. 2013.

[39] T. Li, "Deformation monitoring by multi-temporal InSAR with both point and distributed scatterers," Ph.D. dissertation, Dept. Photogram. Remote Sens. Math., Southwest Jiaotong Univ., Chengdu, China, 2014.

[40] M. Costantini and P. A. Rosen, "A generalized phase unwrapping approach for sparse data," in *Proc. IEEE Int. Geosci. Remote Sens. Symp.*, Hamburg, Germany, Jun./Jul. 1999, pp. 267–269, doi: 10.1109/IGARSS.1999.773467.

[41] Z.-W. Li, X.-L. Ding, D.-W. Zheng, and C. Huang, "Least squares-based filter for remote sensingimage noise reduction," *IEEE Trans. Geosci. Remote Sens.*, vol. 46, no. 7, pp. 2044–2049, Jul. 2008.

[42] "Precipitation and temperature data of Foshan City, China." Accessed: Dec. 15, 2020. [Online]. Available: https://tianqi.911cha.com/foshan/2016.html

[43] A. Mahama, "Improving the solvability of ill-conditioned systems of linear equations by reducing their condition numbers of their matrices," M.S. thesis, Dept. Photogram. Remote Sens. Math., Kwame Nkrumah Univ. Sci. Technol., Kumasi, Ghana, 2015.

[44] R. Zhao, Z.-W. Li, G.-C. Feng, Q.-J. Wang, and J. Hu, "Monitoring surface deformation over permafrost with an improved SBAS-InSAR algorithm: With emphasis on climatic factors modeling," *Remote Sens. Environ.*, vol. 184, pp. 276–287, Oct. 2016, doi: 10.1016/j.rse.2016.07.019.

[45] Q. Chen, "Detecting regional ground deformation by differential SAR interferometry based on permanent scatterers," Ph.D. dissertation, Southwest Jiaotong Univ., Chengdu, China, 2006.

[46] R. Lanari, O. Mora, M. Manunta, J. J. Mallorqui, P. Berardino and E. Sansosti, "A small-baseline approach for investigating deformations on full-resolution differential SAR interferograms," *IEEE Trans. Geosci. Remote Sens.*, vol. 42, no. 7, pp. 1377–1386, Jul. 2004.

[47] Q. T. Zuo, J. X. Ma, and N. K. Zhang, "Verhulst model for the prediction of building settlement and the determination of final settlement at an early start," *Geotech. Eng. Techn.*, vol. 1998, no. 1, pp. 59–62, 1998.

[48] W.-Z. Zhang, Y.-F. Zou, and X.-F. Ren, "Research on logistic model in forecasting subsidence single-point during mining," *J. Mining Saf. Eng.*, vol. 26, no. 1, pp. 486–489, Dec. 2009.

[49] G.-X. Mei and J.-M. Zai, "Forecast method of settlement during the complete process of construction and operation," *Rock Soil Mech.*, vol. 21, no. 4, pp. 322–325, Dec. 2000.

Lingjie Zhu was born in Hunan, China, in 1996. He received the B.S. degree in geomatics and surveying in 2019 from the Changsha University of Science and Technology, Changsha, China, where he is currently working toward the M.S. degree in surveying and mapping.

His research interests include the application of the time-series interferometric synthetic aperture radar technique in highways deformation monitoring.
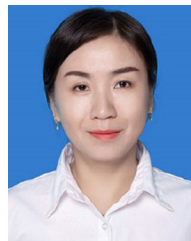
Xuemin Xing was born in Liaoning, China, in 1983. received the B.S. degree in survey and mapping engineering and M.S. degree in geomatics and surveying from Central South University, Changsha, China, in 2005 and 2008, respectively.

From 2016 to 2017, she was a Visiting Scholar with the Department of Environmental Sciences, Macquarie University, Sydney, NSW, Australia. She is currently an Associate Professor with the School of Traffic and Transportation Engineering, Changsha University of Science and Technology, Changsha, China, where she is also a key member of the Laboratory of Radar Remote Sensing Applications. She has authored more than 40 articles and ten inventions. Her research interests include the application of time-series interferometric synthetic aperture radar technique in highway deformation monitoring, deriving spatial–temporal large-scale deformation induced by mining activities and modeling, and the integration of persistent scatterer, corner reflector, and small baseline subset technique.

She is also a reviewer for three international journals and four national journals in China.

Dr. Xing is also a reviewer for three international journals and four national journals in China.

Yikai Zhu was born in Hunan, China, in 1997. He received the B.S. degree in geomatics and surveying in 2018 from the Changsha University of Science and Technology, Changsha, China, where he is currently working toward the M.S. degree in surveying and mapping.

His research interests include the application of the time-series interferometric synthetic aperture radar technique in highways deformation monitoring.

Zhihui Yuan (Member, IEEE) was born in Hunan, China, in 1983. He received the B.S. degree in electronic information engineering from Xiangtan University, Xiangtan, China, in 2007, and the Ph.D. degree in communication and information systems from the Institute of Electronics, Chinese Academy of Sciences, Beijing, China, in 2013.

Since 2013, he has been a Lecturer with the School of Electrical and Information Engineering, Changsha University of Science and Technology, Changsha, China. From 2018 to 2019, he was a Visiting Scholar with the Roy M. Huffington Department of Earth Sciences, Southern Methodist University, working with Professor Zhong Lu on InSAR technique. He is the Principal Investigator of the scientific project "Research on Multichannel InSAR Robust DEM Inversion with High Precision for Complicated Terrain" supported by the National Natural Science Foundation of China. His research interests include signal processing and the application of synthetic aperture radar interferometry, phase unwrapping, high-resolution digital elevation model generation, and algorithm design.
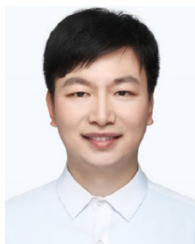
Wei Peng received the Ph.D. degree in geodesy from Central South University, Changsha, China, in 2020.

During October 2017 to October 2018, he was sponsored by the China Scholarship Council to study with Texas State University, San Marcos, TX, USA, as a Joint Ph.D. Student in geography. He is currently a Lecturer with the Changsha University of Science and Technology, Changsha, China. His research interests include GPS and InSAR data processing, and nontectonic deformation.

Qing Xia was born in Liaoning Province, China, in 1987. She received the Ph.D. degree in remote sensing and photogrammetry from the China University of Mining and Technology, Xuzhou, China, in 2017.

Her research interests include environmental monitoring and coastal monitoring in remote sensing. She is currently with the Changsha University of Science and Technology, Changsha, China.